Zonal momentum budget of the Madden-Julian Oscillation: ~~The roles of advection and convective momentum transport~~

Jialin Lin[1], Minghua Zhang[2] and Brian Mapes[1]
[1] **NOAA-CIRES Climate Diagnostics Center, Boulder, CO 80305**
[2] **State University of New York, Stony Brook, NY 11794**
December 2003

Corresponding author address: Dr. Jialin Lin,
NOAA-CIRES Climate Diagnostics Center,
325 Broadway, R/CDC1, Boulder, CO 80305
Email: jialin.lin@noaa.gov

ABSTRACT

Linear, dissipative models have been widely used to study the Madden-Julian Oscillation (MJO). The mechanical damping has been shown to be an important parameter for the growth rate and phase speed of the simulated intraseasonal oscillations. However, because there was no observations on the sources and strength of mechanical damping in the MJO, choices of the damping strength in the models vary over a wide range from highly viscous to totally inviscid. This observational study examines the sources and strength of mechanical damping in the MJO by calculating its zonal momentum budget using 15 years (1979-1993) of daily NCEP/NCAR and ECMWF reanalyses data. Uncertainties in budget estimates are significantly reduced by comparing two different reanalyses, and by constructing long-term composites and considering only the statistically significant signals.

The results show that the MJO is a highly viscous oscillation, with a 3-5 day time-scale damping both in the upper troposphere and in the lower troposphere above the boundary layer. The damping in the upper troposphere is mainly caused by linear advections associated with the strong (about 0.2 day^{-1}) time-mean zonal divergence and the strong time-mean vertical motion in the warm pool region. The damping in the lower troposphere is caused by the convective momentum flux convergence and the nonlinear meridional advection. Meridionally, the damping is confined near the equator between 10N and 10S.

1. Introduction

Discovered by Madden and Julian (1971, 1972), the Madden-Julian Oscillation (MJO) is the dominant intraseasonal mode of variability in tropical convection and circulation (e.g. Weickmann et al. 1985, Lau and Chan 1985, Salby and Hendon 1994, Wheeler and Kiladis 1999). It affects a wide range of tropical weather such as the onset and breaks of the Indian and Australian summer monsoons (e.g. Yasunari 1979, Hendon and Liebmann 1990), and the formation of tropical cyclones (e.g. Nakazawa 1986, Liebmann et al. 1994). It also drives teleconnections to the extratropics (e.g., Lau and Phillips 1986, Winkler et al. 2001) and impacts some important extratropical weather (e.g. Higgins and Mo 1997, Higgins et al. 2000). On a longer timescale, the MJO is observed to trigger or terminate some El Nino events (e.g. Kessler et al. 1995, Takayabu et al. 1999, Bergman et al. 2001). Therefore, the MJO is important for both extended-range weather prediction and long-term climate prediction.

Tropical intraseasonal variability is poorly simulated in general circulation models (GCMs). Typically, simulated phenomena are too weak and propagate too fast (e.g. Hayashi and Sumi 1986, Hayashi and Golder 1986, 1988, 1993, Lau et al. 1988, Slingo et al. 1996). To solve this problem, many theoretical studies have examined the feedback mechanisms which may affect the MJO's amplitude and phase speed, especially the wave-heating feedback mechanisms. Different types of heating parameterizations have been studied, such as wave-CISK (Convective Instability of the Second Kind; e.g. Lau and Peng 1987; Chang and Lim 1988), frictional wave-CISK (e.g. Wang 1988; Salby et al. 1994), WISHE (Wave Induced Surface Heat Exchange; (e.g. Emanuel

1987; Neelin et al. 1987), charge-discharge (e.g. Blade and Hartmann 1993; Hayashi and Golder 1997), and cloud-radiation interaction (Raymond 2001).

In these theoretical studies, linear, dissipative models were often used. The momentum equation was often linearized about a state at rest, neglecting the advective tendency:

$$\frac{\partial u'}{\partial t} = -\frac{\partial \phi'}{\partial x} + fv' - \epsilon u' \tag{1}$$

$$\frac{\partial v'}{\partial t} = -\frac{\partial \phi'}{\partial y} - fu' - \epsilon v' \tag{2}$$

where u is the zonal wind, v is the meridional wind, ϕ the geopotential height, and f the Coriolis parameter. The mechanical damping is usually represented as a Raleigh friction with a time-scale of ϵ^{-1}. In addition to the different kinds of heating parameterizations, the mechanical damping has also been shown to be important for the growth rate and phase speed of the simulated intraseasonal oscillations. When adding a strong damping to the free Kelvin waves, Chang (1977) found that the damping can significantly increase the intrinsic vertical wavelength and decrease the intrinsic phase speed. In a wave-CISK type model, Chao (1987) found that the phase speed of the simulated intraseasonal oscillation decreases with increasing damping. In a WISHE model of the MJO, Neelin et al. (1987) found that the growth rate of the unstable Kelvin modes significantly decreases with increasing mechanical damping, and this was later confirmed by Neelin and Yu (1994) and Goswami and Rao (1994). However, because there was no observational study on the magnitude and sources of mechanical damping in the MJO, the choices of damping magnitude in the theoretical

models varied over a wide range, from highly viscous (e.g. 1 day in Chao 1987), to weakly viscid (e.g. 25 days in Salby et al. 1994), to totally inviscid (e.g. Xie 1994).

The budget terms which are not explicitly expressed in the linearized Eqs. 1 - 2 include the advective tendency and the effect of convective momentum transport (CMT, also called "cumulus friction" in some previous studies), and therefore they are the possible sources of mechanical damping. In the MJO models which did use a strong damping, the source of the damping was usually assumed to be the CMT. CMT was shown to be important for the synoptic-scale waves in both the momentum budget (Stevens 1979) and the vorticity budget (e.g. Reed and Johnson 1974; Shapiro 1978; Stevens 1979; Tollend and Esbenson 1982; see review by Sui and Yanai 1986). For the MJO, the importance of CMT was also shown by two recent observational studies (Houze et al. 2000; Tung and Yanai 2002a,b). Using Doppler radar data collected aircraft and ship radars during TOGA COARE, Houze et al. (2000) studied the mesoscale momentum transport in the "super convective systems" in different phases of the MJO event. They found that the mesoscale momentum transport provides damping to the zonal wind in the westerly onset phase, but acceleration during the westerly wind burst phase. Using TOGA COARE sounding array momentum budgets, Tung and Yanai (2002a,b) studied the area-averaged CMT, which includes both the convective-scale momentum transport and the mesoscale momentum transport (see Carr and Bretherton 2001, Tung and Yanai 2002a, and Lin and Mapes 2004 for discussions on the physics of CMT). They found that the area-averaged CMT is strongly modulated by the MJO event, and provides acceleration in the westerly

onset phase, but damping in the westerly wind burst phase, which is in opposite sign to the effect of mesoscale momentum transport. In these two studies, the magnitude of CMT effect was not compared with those of the other momentum budget terms at the MJO time-scale, and the equivalent damping strength was not estimated. Furthermore, Weickmann et al. (1997) calculated the vertically-integrated angular momentum budget for the MJO, and found that the advective tendency is a dominant budget term. This suggests that the advective tendency may be another important source of mechanical damping.

The purpose of this study is to evaluate the sources and strength of mechanical damping in the observed MJO by calculating the MJO momentum budget using 15 years of daily NCEP/NCAR and ECMWF reanalyses. Because the MJO circulation near the equator is dominated by the zonal wind, we focus on the zonal momentum budget. The main budget uncertainties associated with pressure gradient forces and advection terms are reduced by (1) comparing between NCEP and ECMWF reanalyses, whose consistencies gave us more confidence, and (2) constructing long-term (15 years) MJO composite and considering only the statistically significant signals, which are likely real signals unless the reanalyses have errors coherent with the MJO.

The datasets used in this study are described in section 2. The time filtering and intraseasonal composite (regression) methods are described in section 3. The zonal momentum budget results are reported in section 4. Summary and discussions are given in section 5.

2. Data

The datasets used include 15 years (1979-1999) of daily reanalyses data from two different centers: NCEP and ECMWF. The variables used include upper air wind, geopotential height, and vertical pressure velocity. The horizontal resolution is 2.5 degree longitude by 2.5 degree latitude. Zonal momentum budget is calculated for both reanalyses following Carr and Bretherton (2001). The zonal momentum equation can be written:

$$\frac{\partial u}{\partial t} = -u\frac{\partial u}{\partial x} - v\frac{\partial u}{\partial y} - \omega\frac{\partial u}{\partial p} + f(y)v - \frac{\partial \phi}{\partial x} + X \tag{3}$$

where u is the zonal wind, v the meridional wind, ω the vertical pressure velocity; x and y are E-W and N-S distance, f the Coriolis parameter, and ϕ the geopotential. Here X represents accelerations due to all subgrid-scale processes. In the free troposphere (above the effects of boundary layer turbulence eddies), over the open ocean (away from the effects of topographically induced gravity waves), it is reasonable to assume that convective momentum transport is the dominant subgrid-scale process. Under this assumption, we can write:

$$X = \frac{\partial}{\partial p} < u'\omega' > \tag{4}$$

where $<\quad>$ denotes an ensemble average at a given pressure level, and primes denote the local perturbation from the ensemble average. In this way, we define X to be the acceleration of the zonal flow due to the convective momentum flux convergence.

Each budget term of Eq. 3 was calculated using daily data at each 2.5 degree longitude by 2.5 degree latitude grid. Derivatives were evaluated using central difference

scheme. The results were then averaged to pentad data along the equator (between 5N and 5S) with a zonal resolution of 10 degree longitude.

For constructing the MJO composite, we also used 15 years (1979-1993) of pentad CMAP precipitation data (Xie and Arkin 1997). The horizontal resolution is also 2.5 degree longitude by 2.5 degree latitude. We averaged the data along the equator (between 5N and 5S) with a zonal resolution of 5 degree longitude.

3. Method

The MJO is a broad-band phenomenon, with an averaged period of 45 days but a fairly wide spread from 20 to 80 days (see review by Madden and Julian 1994). Its deep convection signal is dominated by wavenumber 1-6, while its circulation signal is dominated by wavenumber 1 (e.g. Salby and Hendon 1994, Wheeler and Kiladis 1999). The variance of its deep convection signal has two centers: western Pacific and eastern Indian Ocean, and over these two centers, the MJO propagates eastward with a slow phase speed of about 5 m/s (e.g. Wheeler and Kiladis 1999, Lin et al. 2003).

These characteristics were used to isolate the MJO signal. Lin et al. (2003) discussed the different methods used in previous observational and modeling studies. The different methods often give qualitatively similar results in terms of propagation characteristics and phase difference among different variables. This consistency is apparently because strong intraseasonally filtered deep convection fluctuations along the equator are dominated, both in number and strength, by coherent eastward prop-

agating events (Wang and Rui 1990). Linear composite methods used in most of the previous studies (e.g. phase sum, correlation, regression) are apparently dominated by these strong eastward propagating events. The method used in this study is similar to that used in Lin et al. (2003) and Lin and Mapes (2003). The procedure is as follows:

(1) The zonal means were first removed from all datasets.

(2) The datasets were then filtered using a 30-70 day Murakami (1976) filter, whose response function was shown in Lin et al. (2003). The central frequency corresponds to a period of 45 day. The half amplitude is at periods of 30 day and 70 day. We also tested the Lanczos filter (Duchan 1979), and the results were not sensitive.

(3) For the master MJO index, we filtered the CMAP precipitation in time as above, and also in space, retaining wavenumbers 1-6.

(4) To study the MJO phenomena in its two centers of variance, we averaged the datasets in two boxes: a western Pacific box between 150-160E and 5N-5S, and an eastern Indian Ocean box between 80-90E and 5N-5S. For each box, an MJO composite was constructed using linear regression with respect to the filtered CMAP precipitation at the same box, and the regression coefficient was multiplied by one standard deviation of the filtered CMAP precipitation. The confidence level of linear correlation was estimated following Oort and Yienger (1996).

(5) Regressions were done for all seasons of the year, as well as for individual seasons (December-February, March-May, June-August, and September-November).

4. Results

4.1 Vertical structure of the MJO at the equator

Before examing the MJO zonal momentum budget, we first look at the vertical structure of the MJO, which is important for understanding later the zonal momentum budget. The composite vertical structure of MJO in the western Pacific is shown in Fig. 1 using 15 years (1979-1993) of NCEP reanalysis data averaged between 5N-5S and 150-160E. The time lag is with respect to the time of maximum precipitation. The time evolution is from the right to the left, showing the local evolution of measured variables as the eastward-moving MJO passes the measurement longitude. The zonal wind u (Fig. 1a) shows a simple two-layer structure with the upper layer out of phase with the lower layer. This two-layer structure is well-known from many previous observations (e.g. Madden and Julian 1971, 1972, Weickmann et al. 1985, Knutson and Weickmann 1987). However, an interesting feature which did not bring much attention is that the maxima of both the two layers are at a very high altitude, not the 850 mb and 200 mb levels used in many previous MJO studies. The maximum of the lower layer is around 600 mb (just below the 0 C level), while that of the upper layer is around 150 mb (just below the tropopause). It means that at the time of maximum precipitation, the zonal inflow is just below the 0 C level, and the zonal outflow is just below the tropopause. Consistent with this inflow-outflow feature, the vertical motion (Fig. 1b) concentrates in the upper troposphere. For clarity, the two-dimensional flow is plotted using arrows in Fig. 1c. This middle troposphere inflow and near tropopause outflow structure are consistent with the top-heavy heating

profile in the MJO shown in Lin et al. (2003). Therefore, the MJO is associated with a vertical mode concentrating in the upper half of the troposphere.

The vertical motion shows a westward phase tilt with height. It develops first in the lower troposphere, and then shifts upward as it intensifies. This westward phase tilt of vertical motion is consistent with the westward phase tilt of the associated heating anomaly shown in Lin et al. (2003), which is caused by vertical phase tilts of convective heating in the earlier stages, and stratiform heating in the later stages.

The geopotential height Z (contours in Fig. 1c) has a large amplitude in the near-tropopause outflow layer but a small amplitude in the middle-troposphere inflow layer. Z lags u at both the inflow and outflow layers. The phase differences is about 5 days in the outflow layer and 10 days in the inflow layer. The phase difference in the upper layer is smaller than those found by Kiladis and Weickmann (1992) and Hsu (1996). The reason is that we removed the zonal mean component from all datasets while they didn't, and our test using data retaining zonal mean showed that the zonal mean component in geopotential height increases the u and Z phase difference in western Pacific (not shown).

Composites constructed using 15 years (1979-1993) of ECMWF reanalysis data show similar wave structure as the NCEP data (Fig. 2). We also checked the composites for each individual seasons (DJF, MAM, JJA and SON). The wave structures are generally similar to the all-seasons composites.

In summary, the equatorial wave structure of the MJO has the following three characteristics:

(1) It is associated with a vertical mode concentrated in the upper half of the troposphere, with middle-troposphere inflow and near-tropopause outflow at the time of maximum precipitation.

(2) The vertical motion has a westward phase tilt with height.

(3) Geopotential height lags zonal wind by about 5-10 days at both the inflow and outflow layers.

The phase difference between u and Z has implications for the zonal momentum budget. Eq. 1 suggests that when the damping is zero, the balance near the equator is simply between the local tendency and the pressure gradient force. In a neutral wave, this balance leads to an in-phase relationship between u and Z. The observed u-Z phase difference in the MJO suggests that some damping terms may contribute to the zonal momentum budget. In order to know exactly what these "extra" terms are, in the next section we directly examine the zonal momentum budget.

4.2 Zonal momentum budget of the MJO

From Eq. 3, we can write the MJO anomalous zonal momentum equation:

$$\frac{\partial \widetilde{u}'}{\partial t} = -\frac{\partial \widetilde{\phi}'}{\partial x} + \widetilde{fv}' + (-u\widetilde{\frac{\partial u}{\partial x}}' - v\widetilde{\frac{\partial u}{\partial y}}' - \omega\widetilde{\frac{\partial u}{\partial p}}') + \widetilde{X}' \tag{5}$$

where tilde denotes deviation from zonal mean, prime denotes 30-70 day temporally filtered anomaly. The MJO zonal momentum budget terms at the equator (averaged between 150E-160E and 5N-5S) are shown in Figs. 3 and 4 for NCEP and ECMWF reanalyses, respectively. The Coriolis force is small near the equator and is not shown.

The two different reanalyses show similar patterns for each of the three budget terms, giving us more confidence in the results. Moreover, only signals with correlation above the 95% confidence level are plotted in Figs. 3 and 4. These signals are likely real unless there are errors in the reanalyses which are systematically coherent with the MJO. In the upper troposphere, the dominant balance is between the pressure gradient force and the advective tendency. The local tendency is very small, as well as the budget residual. In the lower troposphere, the advective tendency and the budget residual are of similar amplitude as the local tendency and pressure gradient force. The MJO zonal momentum budgets for each individual seasons are similar to the all-season results (not shown). Therefore, the advective tendency is important for the MJO zonal momentum budget in both the upper and the lower tropospheres, while the budget residual is important in the lower troposphere.

The budget residual (Figs. 3d, 4d) shows a two-layer structure, with the residual near the tropopause out of phase with that in the lower troposphere. This is consistent with the vertical structure of budget residual in the TOGA COARE MJO events observed by Tung and Yanai (2002b, their Figs. 8b, 9b). During the westerly wind burst, the budget residual provides a damping to the zonal wind, which is also consistent with the TOGA COARE results. These results suggest that the budget residual from both reanalyses do represent the effect of CMT, and hereafter we'll call the budget residual convective momentum flux convergence (CMFC) as defined in Eq. 4.

The large contribution of advective tendency to the MJO zonal momentum budget

is intriguing and next we examine what cause this strong advection. The zonal, meridional and vertical components of the advective tendency are shown in Figs. 5a, b and c, respectively. The large advection tendency in in the upper troposphere is mainly contributed by zonal advection (Fig. 5a) and vertical advection (Fig. 5c), while that in the lower troposphere is mainly contributed by meridional advection (Fig. 5b). Each of these components contain both linear and nonlinear effects, which can be decomposed into (see Appendix):

$$-\widetilde{u\frac{\partial u}{\partial x}}' = -[\widetilde{u}]\frac{\partial \widetilde{u}'}{\partial x} - \widetilde{u}'\frac{\partial [\widetilde{u}]}{\partial x} + other\ terms \quad (6)$$

$$-\widetilde{v\frac{\partial v}{\partial y}}' = -[\widetilde{v}]\frac{\partial \widetilde{v}'}{\partial y} - \widetilde{v}'\frac{\partial [\widetilde{v}]}{\partial y} + other\ terms \quad (7)$$

$$-\widetilde{\omega\frac{\partial u}{\partial p}}' = -[\widetilde{\omega}]\frac{\partial \widetilde{u}'}{\partial p} - \widetilde{\omega}'\frac{\partial [\widetilde{u}]}{\partial p} + other\ terms \quad (8)$$

where [ ] denotes time-mean. On the righthand side of each equation, the first two terms are linear advection terms associated with time-mean zonal asymmetric flow, while the other terms include the linear terms associated with zonal-mean and the nonlinear terms (see Appendix). The first two linear terms were calculated from the corresponding time-mean and the MJO anomalies, and the other terms were derived as the residual. For the zonal advection and the vertical advection, the corresponding time-mean was taken to be the 15-year mean. For the meridional advection, because there is a strong seasonal variation in meridional wind, the time-mean was taken to be 15-year seasonal mean for one season, using DJF here as an example.

First we look at the decomposition of the zonal advection (Fig. 6) and the vertical advection (Fig. 7), which are important in the upper troposphere. The zonal advec-

tion (Fig. 6) is dominated by the first two linear terms, both of which contribute substantially to the budget. The vertical advection (Fig. 7) is also dominated by the first two linear terms, especially $-[\widetilde{\omega}]\frac{\partial \widetilde{u}'}{\partial p}$ (Fig. 7a). Therefore, the zonal momentum budget of the MJO is basically linear in the upper troposphere. This is consistent with the finding of Weickmann et al. (1997) that the vertically-integrated MJO angular momentum budget is basically linear, because the vertically-integrated momentum budget is mainly contributed by the upper troposphere.

Next we look at the decomposition of the the meridional advection (Fig. 8), which is important in the lower troposphere. The meridional advection is dominated by the nonlinear terms, which may be contributed by the sub-MJO scale oscillations.

In summary, in the MJO zonal momentum budget, the advective tendency is a major budget term in both the upper and lower troposphers, while the CMFC is a major budget term in the lower troposphere. The advective tendency in the upper troposphere is dominated by the linear terms associated with time-mean zonal and vertical motions, including $-[\widetilde{u}]\frac{\partial \widetilde{u}'}{\partial x}$, $-\widetilde{u}'\frac{\partial [\widetilde{u}]}{\partial x}$, and $-[\widetilde{\omega}]\frac{\partial \widetilde{u}'}{\partial p}$, while that in the lower troposphere is dominated by the nonlinear terms. Therefore, near the equator, the MJO zonal momentum budget equation Eq. 5 can be simplified to:

$$\frac{\partial \widetilde{u}'}{\partial t} = -\frac{\partial \widetilde{\phi}'}{\partial x} - [\widetilde{u}]\frac{\partial \widetilde{u}'}{\partial x} - \widetilde{u}'\frac{\partial [\widetilde{u}]}{\partial x} - [\widetilde{\omega}]\frac{\partial \widetilde{u}'}{\partial p} - v\widetilde{\frac{\partial u}{\partial y}}' + \widetilde{X}' \tag{9}$$

4.3 Understanding the linear advection terms in the upper troposphere

The dominant linear advection terms in the upper troposphere own their existence to the time-mean zonal wind $[\widetilde{u}]$, zonal divergence $\frac{\partial[\widetilde{u}]}{\partial x}$, and vertical velocity $[\widetilde{\omega}]$. To help understanding these terms, we plot the 15 year (1979-1993) climatological mean of vertical velocity, zonal divergence, and zonal wind in Fig. 9. For consistency with the MJO anomaly, we plot here the zonal asymmetric components, but the zonal means are actually much smaller. The warm pool region has the strongest climatological deep convection in the world. The deep convection is associated with strong upward motion (Fig. 9a). The vertical velocity profile is very top-heavy, and is therefore associated with strong upper-level zonal divergence concentrating in a thin layer near the tropopause (Fig. 9b). The upper-level zonal wind over the warm pool is easterly (Fig. 9c), which is presumably associated with the Gill (1980) pattern associated with a stationary heating source. The wind is strong within a thin layer near the tropopause because the zonal divergence is concentrated in this layer. Fig. 9 only shows the annual mean, so the upper-level upward motion and zonal divergence are weaker over the eastern Indian Ocean. The long-term composite seasonal variation of upper-level vertical velocity, zonal divergence, and zonal wind (Fig. 10) show that they are actually very strong over the eastern Indian Ocean during northern summer.

When the MJO travels in such a large-scale environment: (1) $-[\widetilde{u}]\frac{\partial\widetilde{u}'}{\partial x}$ (Fig. 6a) lags $\widetilde{u}'$ (Fig. 1a) by a quarter cycle because the time-mean upper-level wind is easterly over the warm pool (Fig. 9c), and it advects the anomalous zonal wind gradience in the MJO. (2) $-\widetilde{u}'\frac{\partial[\widetilde{u}]}{\partial x}$ (Fig. 6b) is out of phase with $\widetilde{u}'$ because the time-mean upper level zonal divergence is positive over the warm pool (Fig. 9b), and it is advected by

the zonal wind anomaly in the MJO. (3) $-[\widetilde{\omega}]\frac{\partial \widetilde{u}'}{\partial p}$ (Fig. 7a) is out of phase with the upper-level $\widetilde{u}'$ (Fig. 1a) because zonal wind shear $\frac{\partial \widetilde{u}'}{\partial p}$ is in phase with upper-level $\widetilde{u}'$ and the time-mean vertical motion is upward (negative $[\widetilde{\omega}]$, Fig. 9a).

Why, then, is the local tendency much smaller than the advective tendency? We can understand this using a simple scale analysis. The basic scales for the MJO and the time-mean flow over the warm pool are:

$T \approx 40$ days	period
$L \approx 4 \times 10^7$ m	zonal wavelength
$[\widetilde{u}] \approx 10$ m/s	time-mean upper-level zonal wind
$\frac{\partial [\widetilde{u}]}{\partial x} \approx 0.2\ day^{-1}$	time-mean upper-level zonal divergence

From these scales we can estimate the magnitude of the local tendency and the dominant linear zonal advection terms:

$$\begin{aligned} \frac{\partial \widetilde{u}'}{\partial t} &\approx 2\widetilde{u}'/(0.5T) \approx \widetilde{u}'/(10\ \ days) \\ -[\widetilde{u}]\frac{\partial \widetilde{u}'}{\partial x} &\approx [\widetilde{u}] \times 2\widetilde{u}'/(0.5L) \approx \widetilde{u}'/(10\ \ days) \\ -\widetilde{u}'\frac{\partial [\widetilde{u}]}{\partial x} &\approx \widetilde{u}'/(5\ \ days) \end{aligned}$$

Therefore, the linear zonal advection terms is larger than the local tendency. Because the vertical advection terms enhance the zonal advection terms, the total advective tendency (Fig. 3c), when scaled using $\widetilde{u}'$ (Fig. 1a), is equivalent to a time-scale of 2-3 days, which is much shorter than the 10 days time-scale of local tendency. Therefore, the dominant balance between advective tendency and pressure gradient force in the upper troposphere is a physically robust feature for the MJO.

In summary, over the warm pool region, the strong climatological deep convection is associated with strong upward motion, strong upper-level zonal divergence, and strong upper-level easterly wind. Simple scale analysis shows that the magnitudes of these time-mean flows are bound to cause an advective tendency much larger than the local tendency at the MJO time-scale, leading to the dominant balance between advective tendency and pressure gradient force.

4.4 Equivalent linear damping

To get quantitative estimates of the equivalent linear damping strength in the MJO, we regressed the MJO anomalies of the budget terms to the MJO zonal wind anomaly (Fig. 11). When a budget term is in phase (out of phase) with the zonal wind, it provides a forcing (damping). The unit of the regression coefficient is 1/day, i.e., the inverse of the coefficient gives the damping time-scale in the unit of days. The corresponding correlation coefficient indicates how well the budget term is represented by a linear damping.

The pressure gradient force (Fig. 11a) provides a 2-3 days forcing in the upper troposphere (150-300 mb), and a 3-5 days forcing in the lower troposphere (below 700 mb). This strong forcing can not be balanced by the local tendency, which, as shown in section 4.3, has a time-scale of about 10 days. The Coriolis force is also small near the equator. Therefore, some strong dampings are needed to balance the pressure gradient force. In other words, the MJO is a highly viscous oscillation.

In the upper troposphere, the damping mainly comes from the advective tendency

(Fig. 11b), which, as shown in section 4.2, includes $-\widetilde{u}'\frac{\partial[\widetilde{u}]}{\partial x}$ and $-[\widetilde{\omega}]\frac{\partial\widetilde{u}'}{\partial p}$. The CMFC (Fig. 11c) also contributes slightly near the tropopause. In the lower troposphere, the damping comes equally from the advective tendency (the nonlinear meridional advection term) and the CMFC. The linear correlation coefficient is generally large when the regression coefficient is large, suggesting the usefulness of linear damping representation.

It is also important to know the meridional distribution of damping. Fig. 12 shows the meridional distribution at 200 mb of damping due to the advective tendency. The damping is large only near the equator between 10N-10S. This is because the strong upper-level zonal divergence and vertical motion are confined to near the equator. The damping in the lower levels also has its largest value near the equator (not shown).

5. Summary and discussions

This study examined the equatorial wave structure and zonal momentum budget of the MJO. The results are schematically shown in Fig. 13. The equatorial wave structure of the MJO is associated with a vertical mode concentrated in the upper half of the troposphere, with middle-troposphere inflow and near-tropopause outflow at the time of maximum precipitation. The vertical motion has a westward phase tilt with height. Geopotential height lags zonal wind by about 5-10 days at both the inflow and outflow layers.

In the MJO zonal momentum budget, the advective tendency is a major budget

term in both the upper and lower tropospheres, while the CMFC is a major budget term only in the lower troposphere. The advective tendency in the upper troposphere comes from the linear terms associated with time-mean zonal and vertical motions, while that in the lower troposphere comes from the nonlinear meridional advection. The simplified MJO zonal momentum equation is Eq. 9.

The strong linear advection terms in the upper troposphere can be understood from the time-mean flow in the warm-pool region. The warm pool region has the strongest climatological deep convection in the world. The deep convection is associated with strong upward motion ($[\omega] < 0$), strong upper-level zonal divergence ($\partial[u]/\partial x > 0$), and strong upper-level easterly wind ($[u] < 0$). When the MJO travels in such a large-scale environment, at the upper levels, $-[u]\partial u'/\partial x$ lags u' by a quarter cycle, while both $-u'\partial[u]/\partial x$ and $-[\omega]\partial u'/\partial p$ are out of phase with u'. Simple scale analysis shows that the magnitudes of the time-mean flows are bound to cause an advective tendency much larger than the local tendency at the MJO time-scale, leading to the dominant balance between advective tendency and pressure gradient force.

When scaled by the zonal wind anomaly, the advective tendency and the convective momentum flux convergence together provide a 3-5 day time-scale damping to the MJO both in the upper troposphere and in the lower troposphere. Therefore, the MJO is a highly viscous oscillation. The damping is large only near the equator between 10N-10S.

As discussed in the introduction, because there was no observational study on

the sources and strength of mechanical damping in the MJO, the choices of damping strength in the theoretical models varied over a wide range, from highly viscous to totally inviscid. It would be interesting to study the effect of using the observed strong damping on the different wave-heating feedback mechanisms. One possible effect is on the growth rate of the unstable intraseasonal modes. The unstable modes under weak damping may be removed under strong damping, as shown in the WISHE model of Goswami and Rao (1994, their Fig. 5c). Therefore several different feedback mechanisms may need to work together to generate unstable modes (e.g. WISHE plus cloud-radiation feedback). Another possible effect is on the phase speed of the intraseasonal modes. The wave-CISK model of Chao (1987) shows that strong damping reduces the phase speed of the intraseasonal modes, but the effects on other feedback mechanisms need further study.

The main focus of this study is on the sources and strength of mechanical damping in the MJO, so we focus on the budget terms which are out of phase with the zonal wind. However, the budget terms which are in quadrature with the zonal wind, especially the strong $-[\widetilde{u}]\frac{\partial \widetilde{u'}}{\partial x}$ term, are also important for the MJO dynamics. As pointed by Houze et al. (2000), when a force leads (lags) the zonal wind by a quarter cycle, it tends to shorten (prolong) the period of the oscillation. Therefore, $-[\widetilde{u}]\frac{\partial \widetilde{u'}}{\partial x}$ tends to prolong the period of the MJO. This term exists because the MJO always travels in the strong time-mean tropical easterly jet (Fig. 10c), which is associated with both the Walker circulation and the local Hadley circulation.

Acknowledgments

We gratefully thank Klaus Weickmann and George Kiladis for carefully reading an early version of the manuscript and making very helpful comments. We also thank Don Hooper for assistance in reading the reanalyses data.

Appendix. Decomposition of the advection terms

Because the MJO anomaly in this study does not include the zonal mean, decomposition of the advection terms is more complex than when zonal mean is retained. Following Peixoto and Oort (1992, pp61-64), a quantity A can be decomposed into:

$$A = [\overline{A}] + [\widetilde{A}] + \overline{A}' + \widetilde{A}' \tag{A1}$$

where overbar represents zonal mean, tilde represents deviation from the zonal mean (zonal asymmetric component), bracket represents time mean, and prime represents deviation from the time mean. It can be derived that:

$$\begin{aligned}\widetilde{AB}' = ([\widetilde{A}]\widetilde{B}' + [\widetilde{B}]\widetilde{A}') + ([\overline{A}]\widetilde{B}' + [\overline{B}]\widetilde{A}') + ([\widetilde{A}]\overline{B}' + [\widetilde{B}]\overline{A}') \\ +(-\overline{[\widetilde{A}]\widetilde{B}'} - \overline{[\widetilde{B}]\widetilde{A}'} + \widetilde{A'B'} - [\widetilde{A'B'}])\end{aligned} \tag{A2}$$

On the right hand of the equation, the terms on the first line are the linear terms, among which the first two are associated with time-mean zonal asymmetric component, and are calculated in Eqs. 6 and 8. The third and fourth are associated with time-mean zonal-mean component. The fifth and sixth are associated with temporally filtered zonal-mean component. The terms on the second line are the nonlinear terms. When considering only the 30-70 day anomalies, the nonlinear terms will in-

clude some more terms corresponding to interaction with other time-scales.

REFERENCES

Bergman, J. W., H. H. Hendon, K. M. Weickmann, 2001: Intraseasonal Air-Sea Interactions at the Onset of El Nino. *Journal of Climate*, 14, 1702-1719.

Carr, Matthew T., Bretherton, Christopher S. 2001: Convective Momentum Transport over the Tropical Pacific: Budget Estimates. *J. Atmos. Sci.*, **58**, 1673-1693.

Chang, C. P., 1977: Viscous internal gravity waves and low-frequency oscillations in the tropics. *J. Atmos. Sci.*, **34**, 901-910.

Chang, C. P., and H. Lim, 1988: Kelvin wave-CISK: A possible mechanism for the 30-50 day oscillations. *J. Atmos. Sci.*, **45**, 1709-1720.

Cho, H.-R., K. Fraedrich, and J. T. Wang, 1994: Cloud clusters, Kelvin wave-CISK , and the Madden-Julian oscillations in the equatorial troposphere. *J. Atmos. Sci.*, **51**, 68-76.

Crum, F. R., and T. J. Dunkerton, 1992: Analytic and numerical models of wave-CISK with conditional heating. *J. Atmos. Sci.*, **49**, 1693-1708.

Duchan, C.E., 1979: Lanczos filtering in one and two dimensions. *J. Appl. Meteor.*, **18**, 1016-1022.

Emanuel, K. A., 1987: An air-sea interaction model of intraseasonal oscillation in the Tropics. *J. Atmos. Sci.*, **44**, 2324-2340.

Gallus, William A., Johnson, Richard H. 1992: The Momentum Budget of an Intense Midlatitude Squall Line. *J. Atmos. Sci.*, **49**, 422-450.

Gill, A. E., 1980: Some simple solutions for heat-induced tropical circulation. *Quart. J. Roy. Meteor. Soc.*, **106**, 447-462.

Hayashi, Y., and A. Sumi, 1986: The 30-40 day oscillation simulated in an"aqua planet" model. *J. Meteor. Soc. Japan.*, **64**, 451-466.

Hayashi, Y., and D. G. Golder, 1986: Tropical intraseasonal oscillations appearing in a GFDL general circulation model and FGGE data. Part I: Phase propagation. *J. Atmos. Sci.*, **43**, 3058-3067.

Hayashi, Y., and D. G. Golder, 1988: Tropical intraseasonal oscillations appearing in a GFDL general circulation model and FGGE data. Part II: Structure. *J. Atmos. Sci.*, **45**, 3017-3033.

Hayashi, Y., and D. G. Golder, 1993: Tropical 40-50 and 25-30-day oscillations appearing in realistic and idealized GFDL climate models and the ECMWF dataset. *J. Atmos. Sci.*, **50**, 464-494.

Hendon, H. H., and B. Liebmann, 1990: A composite study of onset of the Australia monsoon. *J. Atmos. Sci.*, 47, 2227-2240.

Houze, R. A., Chen, S. S., Kingsmill, D. E., Serra, Y., Yuter, S. E. 2000: Convection over the Pacific Warm Pool in relation to the Atmospheric Kelvin-Rossby Wave. *J. Atmos. Sci.*, **57**, 3058-3089.

Hsu, H.-H., 1996: Global view of the intraseasonal oscillation during northern winter. *J. Climate*, **9**, 2386-2406.

Inness, P. M., and D. Gregory, 1997: Aspects of the intraseasonal oscillation simulated by the Hadley Centre Atmosphere Model. *Climate Dyn.*, **13**, 441-458.

Kessler, W. S., and M. J. McPhaden, and K. M. Weickmann, 1995: Forcing of intraseasonal Kelvin waves in the equatorial Pacific. *J. Geophys. Res.*, 100, 10613-10631.

Kiladis, G. N., and K. M. Weickmann, 1992: Circulation anomalies associated with tropical convection during northern winter. *Mon. Wea. Rev.*, **120**, 1900-1923.

Knutson, T. R., and K. M. Weickmann, 1987: 30-60 day atmospheric oscillations: Composite life cycles of convection and circulation anomalies. *Mon. Wea. Rev.*, **115**, 1407-1436.

Lau, K. M., and P. H. Chan, 1985: Aspects of the 40-50-day oscillation during the northern winter as inferred from outgoing longwave radiation. *Mon. Wea. Rev.*, **113**, 1889-1909.

Lau, K. M., and L. Peng, 1987: Origin of low-frequency (intraseasonal) oscillations in the tropical atmosphere. *J. Atmos. Sci.*, **44**, 950-972.

Lau, K.-M., and T. J. Phillips, 1986: Coherent fluctuations of extratropical geopotential height and tropical convection in intraseasonal timescales. *J. Atmos. Sci.*, 43, 1164-1181.

Lau, N. C., I. M. Held, and J. D. Neelin, 1988: The Madden-Julian oscillations in an idealized general circulation model. *J. Atmos. Sci.*, **45**, 3810-3831.

Liebmann, B., H. H. Hendon, and J. D. Glick, 1994: The relationship between t tropical cyclones of the western Pacific and Indian Oceans and the Madden-Julian oscillation. *J. Meteor. Soc. Japan*, 72, 401-411.

Lin, J., B. E. Mapes, M. H. Zhang, and M. Newman, 2003: Stratiform precipitation, vertical heating profiles, and the Madden-Julian Oscillation. *J. Atmos. Sci.*, in press.

Lin, J. L., and B. E. Mapes, 2003: Radiation budget of the tropical intraseasonal oscillations. *J. Atmos. Sci.*, accepted. Available at http://www.cdc.noaa.gov/~jlin

Lin, J., and B. E. Mapes, 2004: Role of convective momentum transport in tropical large-scale circulations. *J. Atmos. Sci.*, to be submitted.

Lindzen, R. D., 1967: Planetary waves on beta-planes. *Mon. Wea. Rev.*, **95**, 441-451.

Madden, R. A., and P. R. Julian, 1971: Detection of a 40-50 day oscillation in the zonal wind in the tropical Pacific. *J. Atmos. Sci.*, **28**, 702-708.

Madden, R. A., and P. R. Julian, 1972: Description of global-scale circulation cells in the tropics with a 40-50 day period. *J. Atmos. Sci.*, **29**, 1109-1123.

Madden, R. A., and P. R. Julian, 1994: Observations of the 40-50-day oscillation -A review. *Mon. Wea. Rev.*, **122**, 814-837.

Mapes, B. E., Wu, X. 2001: Convective Eddy Momentum Tendencies in Long Cloud-Resolving Model Simulations. *J. Atmos. Sci.*, **58**, 517-526.

Matsuno, T., 1966: Quasi-geostrophic motions in the equatorial area. *J. Meteor. Soc. Japan*, 44, 25-43.

Mehta, A. V., and E. A. Smith, 1997: Variability of radiative cooling during the Asian summer monsoon and its influence on intraseasonal waves. *J. Atmos. Sci.*, **54**, 941-966.

Murakami, M., 1979: Large-scale aspects of deep convective activity over the GATE area. *Mon. Wea. Rev.*, **107**, 994-1013.

Nakazawa, T., 1986: Mean features of 30-60 day variations as inferred from 8-year OLR data. *J. Meteor. Soc. Japan*, **64**, 777-786.

Neelin, J. D., I. M. Held, and K. H. Cook, 1987: Evaporation-wind feedback and low-frequency variability in the tropical atmosphere. *J. Atmos. Sci.*, **44**, 2341-2348.

Oort, A. H., and J. J. Yienger, 1996: Observed long-term variability in the Hadley circulation and its connection to ENSO. *J. Climate*, 9, 2751-2767.

Salby, M. L., and H. H. Hendon, 1994: Intraseasonal behavior of clouds, temperature, and motion in the Tropics. *J. Atmos. Sci.*, **51**, 2207-2224.

Slingo, J. M., and Coauthors, 1996: Intraseasonal oscillations in 15 atmospheric general circulation models: Results from an AMIP diagnostic subproject. *Climate Dyn.*, **12**, 325-357.

Stevens, D. E., 1979: Vorticity, momentum, and divergence budgets of synoptic-scale wave disturbances in the tropical eastern Atlantic. *Mon. Wea. Rev.*, **107**, 535-550.

Takayabu, Y .N., Toshio Iguchi, Misako Kachi, Akira Shibata and Hiroshi Kanzawa, 1999: Abrupt termination of the 1997-98 El Nino in response to a Madden-Julian oscillation. *Nature*, 402, 279-282.

Tung, W. W., Yanai, M., 2002a: Convective Momentum Transport Observed during the TOGA COARE IOP. Part I: General Features. *J. Atmos. Sci.*, **59**, 1857-1871.

Tung, W. W., Yanai, M., 2002b: Convective Momentum Transport Observed during the TOGA COARE IOP. Part II: Case Studies. *J. Atmos. Sci.*, **59**, 2535-2549.

Wang, B., 1988: Dynamics of tropical low-frequency waves: An analysis of the moist Kelvin wave. *J. Atmos. Sci.*, **45**, 2051-2065.

Wang, B., and H. Rui, 1990: Synoptic climatology of transient tropical intraseasonal convection anomalies. *Meteor. Atmos. Phys.*, **44**, 43-61.

Weickmann, K. M., G. R. Lussky, and J. E. Kutzbach, 1985: Intraseasonal (30-60 day) fluctuations of outgoing longwave radiation and 250 mb streamfunction during northern

winter. *Mon. Wea. Rev.*, 113, 941-961.

Weickmann, K. M., G. N. Kiladis, and P. D. Sardeshmukh, 1997: The dynamics of intraseasonal atmospheric angular momentum oscillations. *J. Atmos. Sci.*, **54**, 1445-1461.

Wheeler, M., and G. N. Kiladis, 1999: Convectively coupled equatorial waves: Analysis of clouds and temperature in the wavenumber-frequency domain. *J. Atmos. Sci.*, **56**, 374-399.

Wu, X., and M. Yanai, 1994: Effect of vertical wind shear on the cumulus transport of momentum: Observations and parameterization. *J. Atmos. Sci.*, **51**, 1640-1660.

Xie, P., and P. A. Arkin, 1997: Global precipitation: A 17-year monthly analysis based on gauge observations, satellite estimates, and numerical model outputs. *Bull. Amer. Meteor. Soc.*, **78**, 2539-2558.

Yasunari, T., 1979: Cloudiness fluctuations associated with the northern hemisphere summer monsoon. *J. Meteor. Soc. Japan*, 57, 227-242.

Zhang, M. H., and J. L. Lin, 1997: Constrained variational analysis of sounding data based on column-integrated budgets of mass, heat, moisture, and momentum: Approach and application to ARM measurements. *J. Atmos. Sci.*, **54**, 1503-1524.

FIGURE CAPTIONS

Fig. 1 The vertical structure of the MJO anomaly for (a) zonal wind (m/s), (b) vertical velocity (mb/day), and (c) geopotential height (m) for the 15 years (1979-1993) of NCEP reanalysis data averaged over 150E-160E and 5N-5S. Negative values are shaded. The arrows in (c) are the wind vectors whose horizontal component is the zonal wind, and vertical component the vertical velocity.

Fig. 2 Same as Fig. 1 except for the ECMWF reanalysis data.

Fig. 3 Terms of the MJO zonal momentum budget: (a) local tendency $\frac{\partial \widetilde{u}'}{\partial t}$, (b) pressure gradient force $-\frac{\partial \widetilde{\phi}'}{\partial x}$, (c) advection terms $(-\widetilde{u\frac{\partial u}{\partial x}}' - \widetilde{v\frac{\partial u}{\partial y}}' - \widetilde{\omega\frac{\partial u}{\partial p}}')$, and (d) the residual term $\widetilde{X}'$, for 15 years (1979-1993) of NCEP reanalysis data averaged over 150E-160E and 5N-5S. Unit is $ms^{-1}day^{-1}$.

Fig. 4 As in Fig. 3 except for ECMWF reanalysis data.

Fig. 5 As in Fig. 3 except for three advection terms for NCEP reanalysis data: (a) zonal advection $-\widetilde{u\frac{\partial u}{\partial x}}'$, (b) meridional advection $-\widetilde{v\frac{\partial u}{\partial y}}'$, and (c) vertical advection $-\widetilde{\omega\frac{\partial u}{\partial p}}'$.

Fig. 6 As in Fig. 3 except for three components of the zonal advection term for NCEP reanalysis data: (a) $-[\widetilde{u}]\frac{\partial \widetilde{u}'}{\partial x}$, (b) $-\widetilde{u}'\frac{\partial [\widetilde{u}]}{\partial x}$, and (c) other terms.

Fig. 7 As in Fig. 3 except for three components of the vertical advection term for NCEP reanalysis data: (a) $-[\widetilde{\omega}]\frac{\partial \widetilde{u}'}{\partial p}$, (b) $-\widetilde{\omega}'\frac{\partial [\widetilde{u}]}{\partial p}$, and (c) other terms.

Fig. 8 As in Fig. 3 except for three components of the meridional advection term for NCEP reanalysis data for DJF season: (a) $-[\widetilde{v}]\frac{\partial \widetilde{u}'}{\partial y}$, (b) $-\widetilde{v}'\frac{\partial [\widetilde{u}]}{\partial y}$, and (c) other terms.

Fig. 9 Annual mean (a) $[\widetilde{\omega}]$ (mb/day), (b) $\frac{\partial \widetilde{[u]}}{\partial x}$ (1/day), and (c) $[\widetilde{u}]$ (m/s), for 15 years (1979-1993) of NCEP reanalysis data along the equator (5N-5S).

Fig. 10 Seasonal variation of (a) $[\widetilde{\omega}]$ (mb/day) at 300 mb, (b) $\frac{\partial \widetilde{[u]}}{\partial x}$ (1/day) at 150 mb, and (c) $[\widetilde{u}]$ (m/s) at 150 mb, for NCEP reanalysis data along the equator (5N-5S).

Fig. 11 Vertical profile of linear regression coefficient of the MJO (a) pressure gradient force anomaly, (c) advective tendency anomaly, and (e) budget residual anomaly, with respect to the zonal wind anomaly at the same level for 15 years (1979-1993) of NCEP (solid line) and ECMWF (dashed line) reanalyses data averaged over 150E-160E and 5N-5S. The corresponding correlation coefficients are shown in (b), (d), and (f), respectively.

Fig. 12 Meridional profile of (a) linear regression coefficient, and (b) linear correlation coefficient, between the 200 mb MJO advective tendency anomaly and zonal wind anomaly averaged between 150E-160E for 15 years (1979-1993) of NCEP (solid line) and ECMWF (dashed line) reanalyses data.

Fig. 13 Schematic depiction of the time-mean flow over the warm-pool, and the observed MJO wave structure and zonal momentum budget. Regions of enhanced large-scale convection are indicated schematically by the clouds. The dark shading inside the clouds represents the maximum of the diabatic heating. "H" and "L" represent the high and low geopotential height anomalies, respectively. Thin arrows represent the winds. Thick arrows above the MJO wave represent components of zonal momentum budget in the upper troposphere, while those below the MJO wave represent components in the lower troposphere.

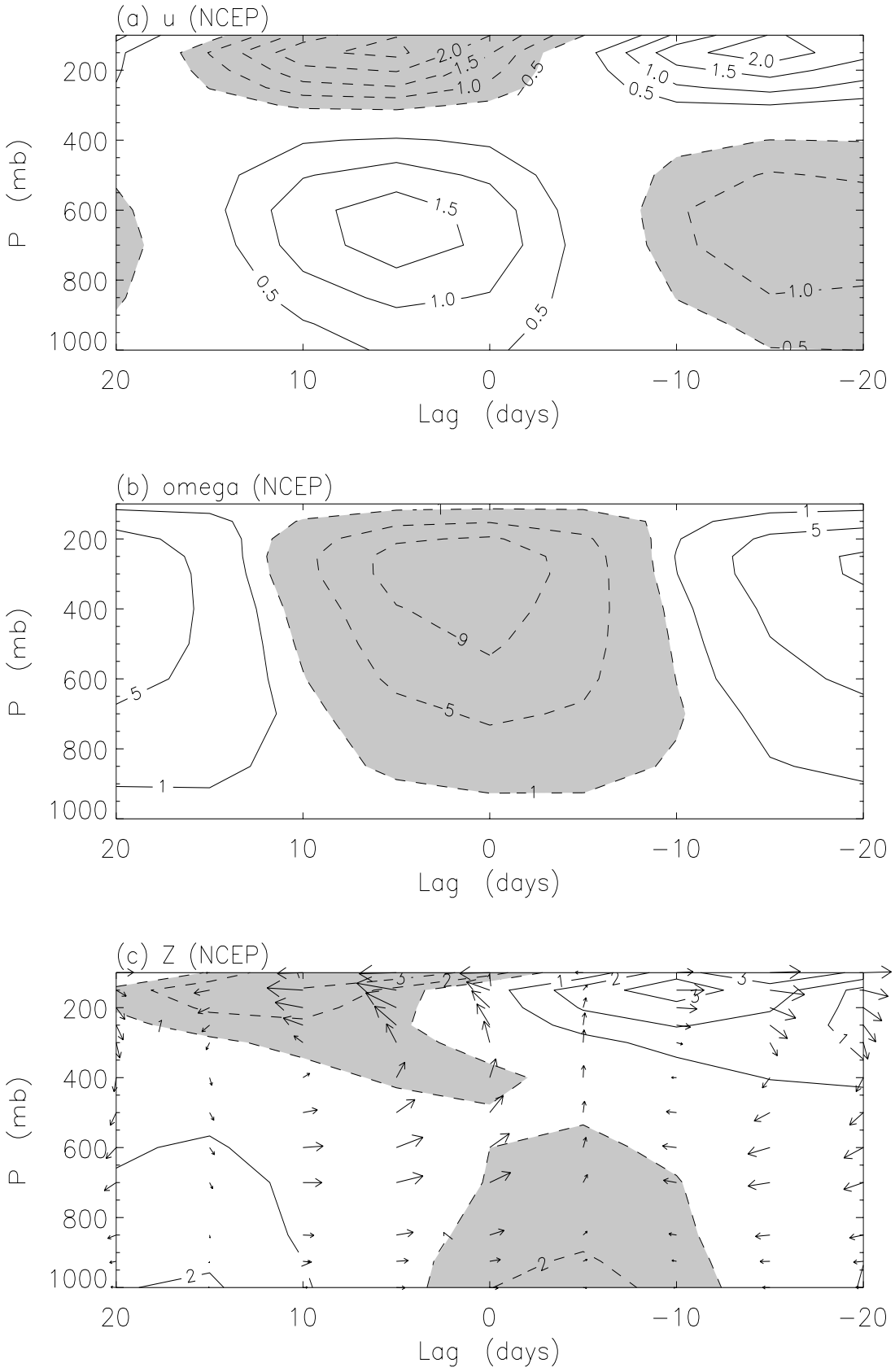
(a) u (NCEP)
P (mb)
200
400
600
800
1000
20
10
0
−10
−20
Lag (days)
(b) omega (NCEP)
P (mb)
Lag (days)
(c) Z (NCEP)
P (mb)
Lag (days)

Figure 1:

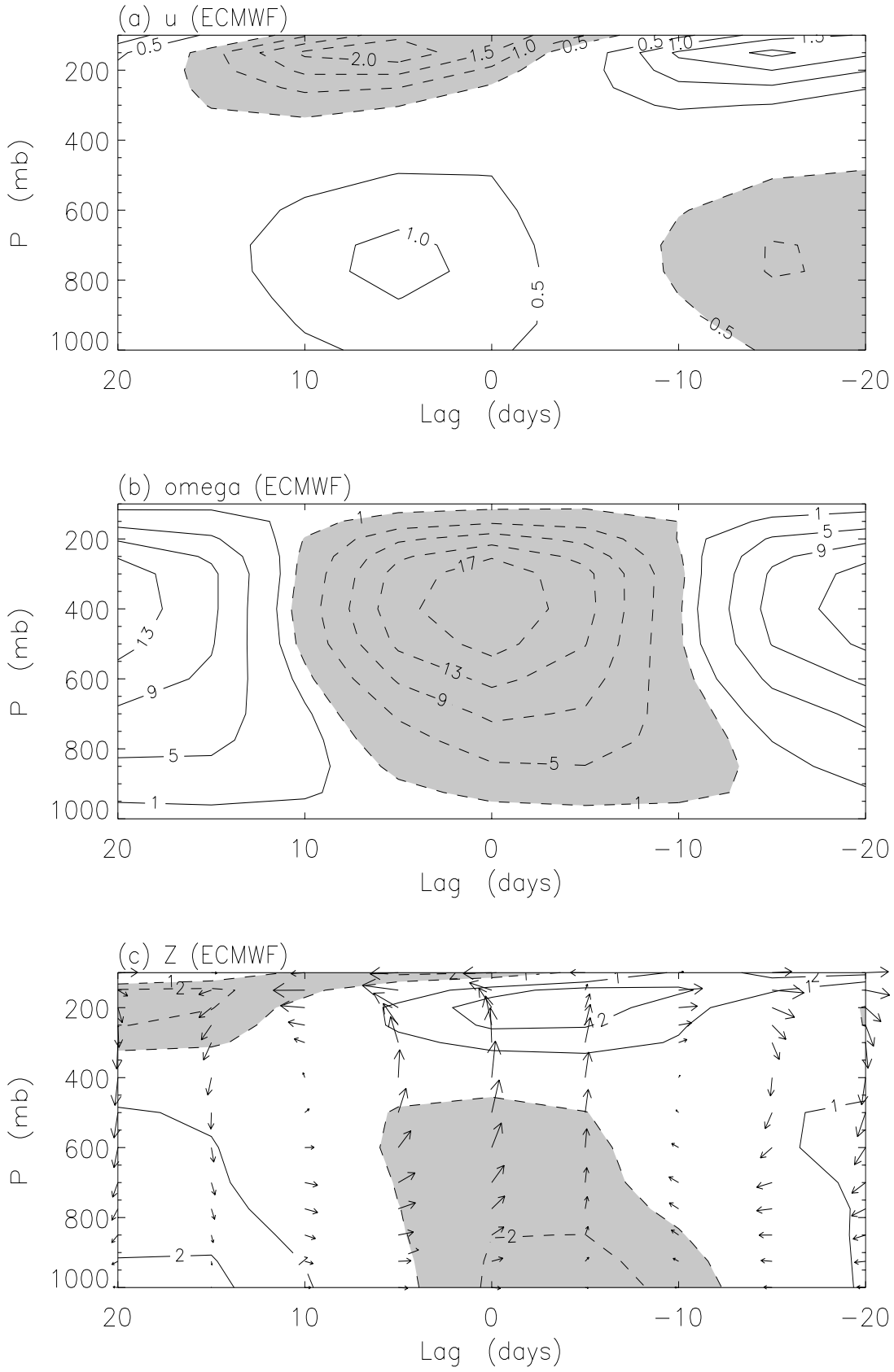
(a) u (ECMWF)
P (mb)
200
400
600
800
1000
20
10
0
−10
−20
Lag (days)
(b) omega (ECMWF)
P (mb)
Lag (days)
(c) Z (ECMWF)
P (mb)
Lag (days)

Figure 2:

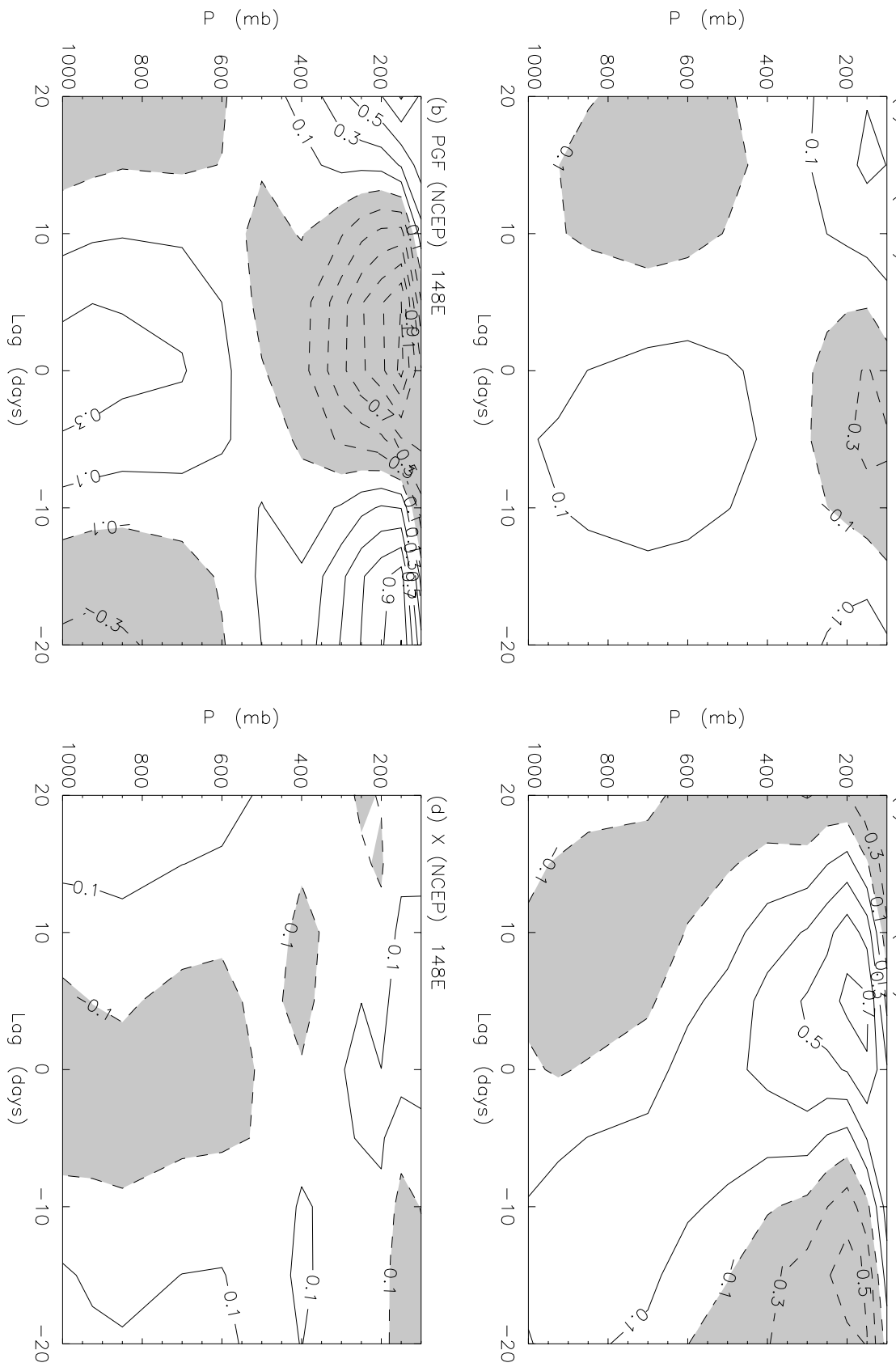
(a) Local (NCEP) 148E
(b) PGF (NCEP) 148E
(c) Advection (NCEP) 148E
(d) X (NCEP) 148E
P (mb)
Lag (days)

Figure 3:

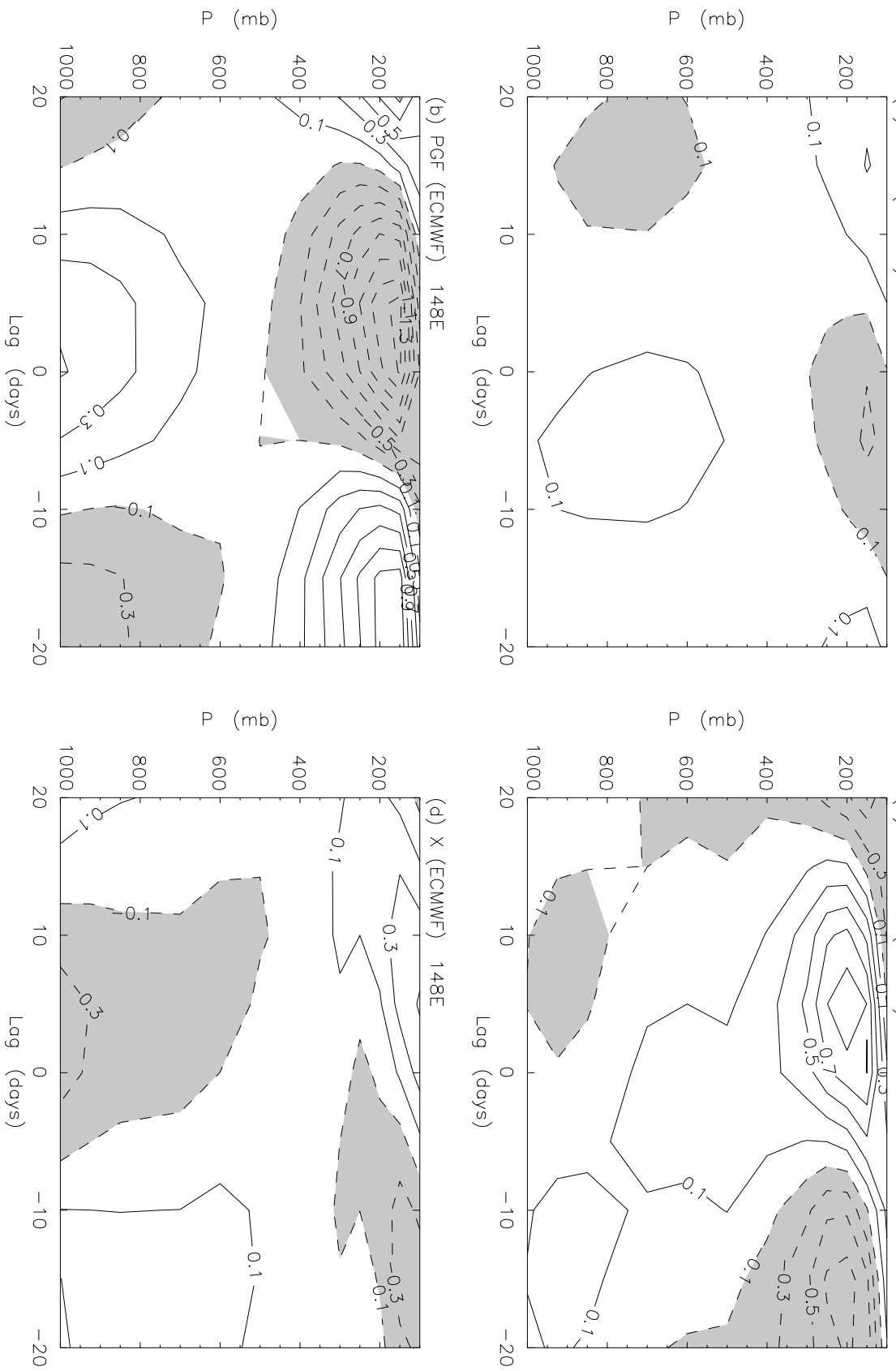
(a) Local (ECMWF) 148E
(b) PGF (ECMWF) 148E
(c) Advection (ECMWF) 148E
(d) X (ECMWF) 148E
P (mb)
Lag (days)

Figure 4:

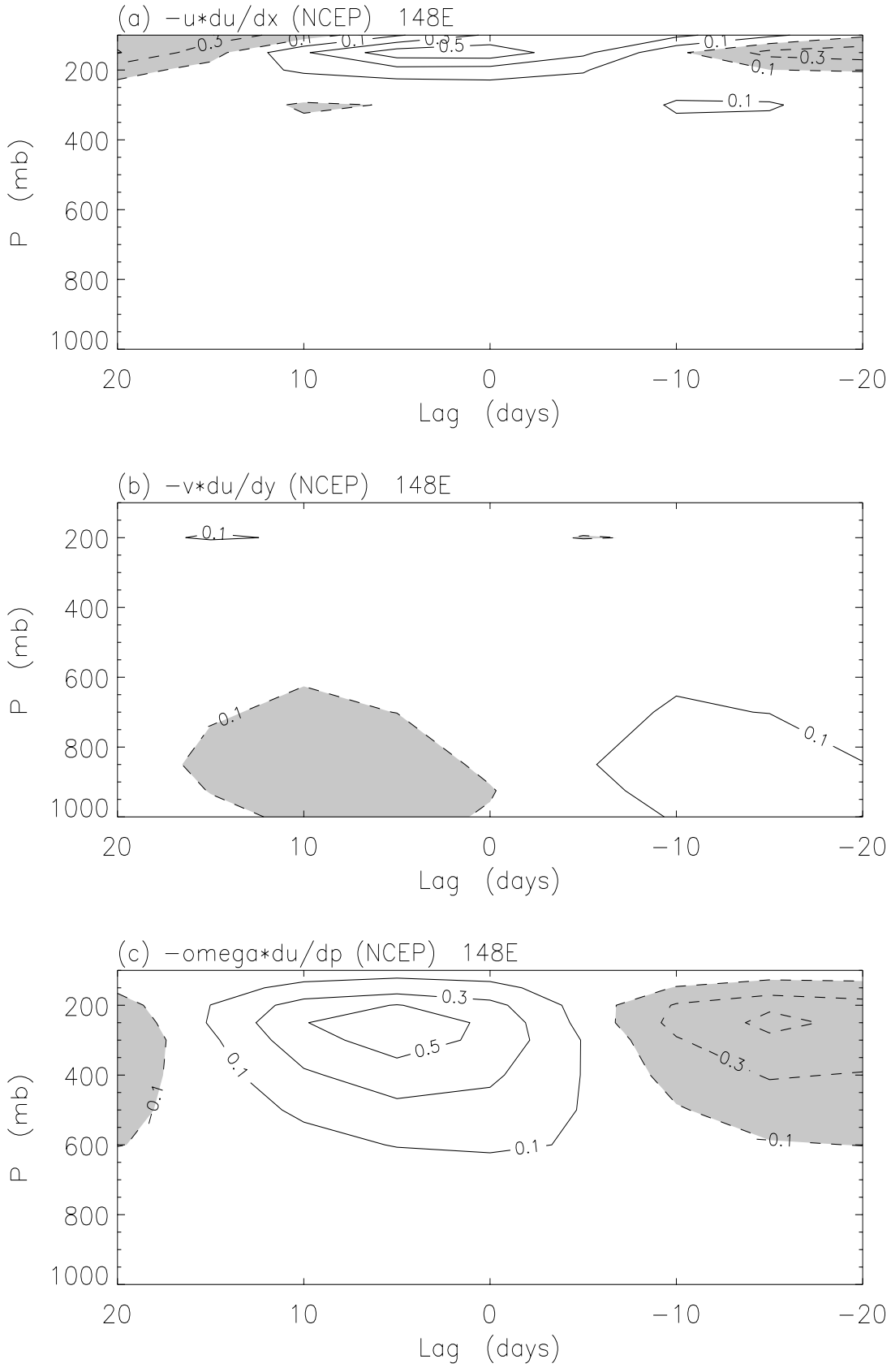
(a) −u*du/dx (NCEP) 148E
(b) −v*du/dy (NCEP) 148E
(c) −omega*du/dp (NCEP) 148E
P (mb)
200
400
600
800
1000
20
10
0
−10
−20
Lag (days)
0.5
0.1
0.3

Figure 5:

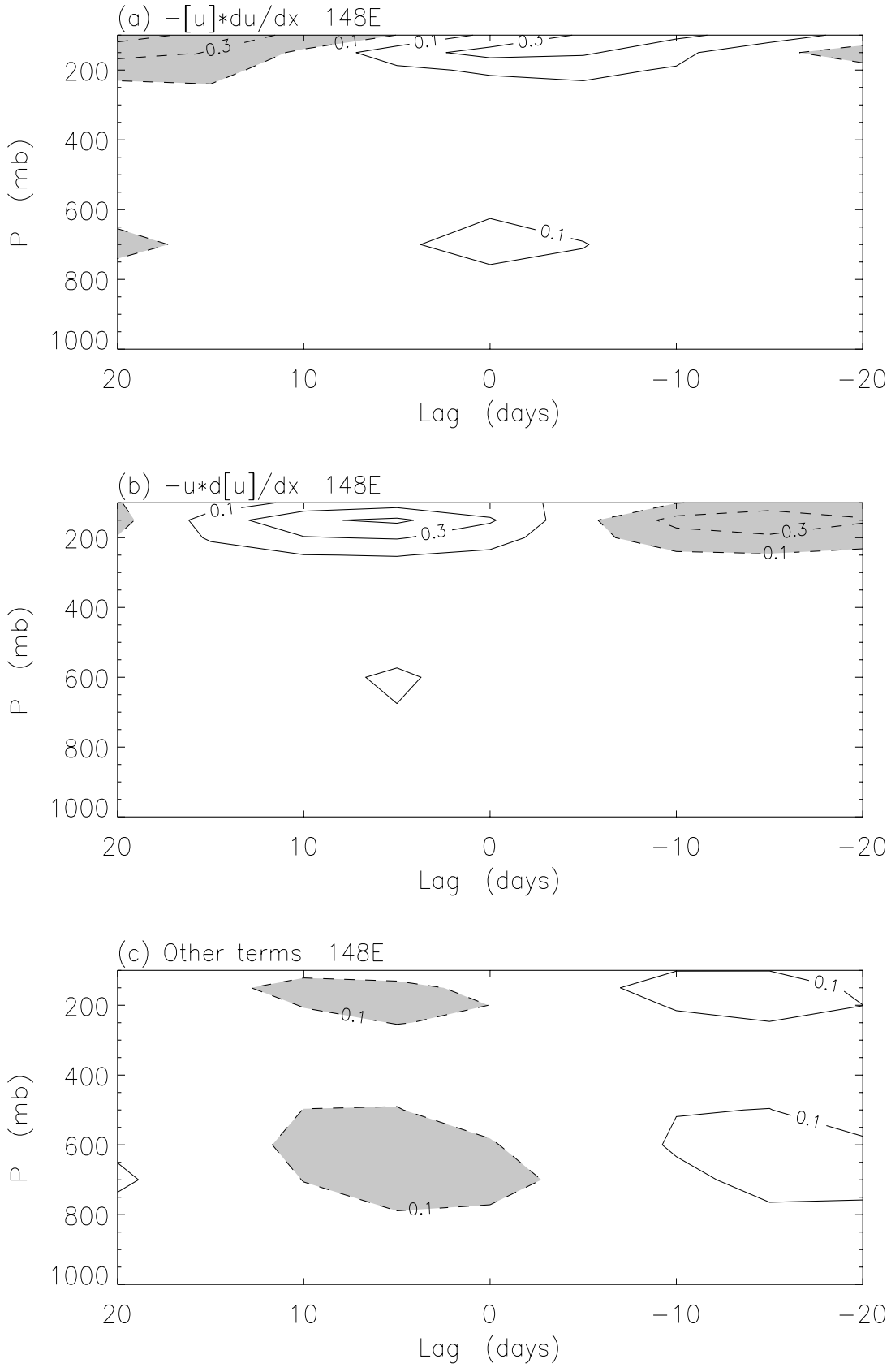
(a) −[u]*du/dx 148E
0.3
0.1
0.1
0.3
0.1
P (mb)
200
400
600
800
1000
20
10
0
−10
−20
Lag (days)
(b) −u*d[u]/dx 148E
0.1
0.3
0.3
0.1
P (mb)
200
400
600
800
1000
20
10
0
−10
−20
Lag (days)
(c) Other terms 148E
0.1
0.1
0.1
0.1
P (mb)
200
400
600
800
1000
20
10
0
−10
−20
Lag (days)

Figure 6:

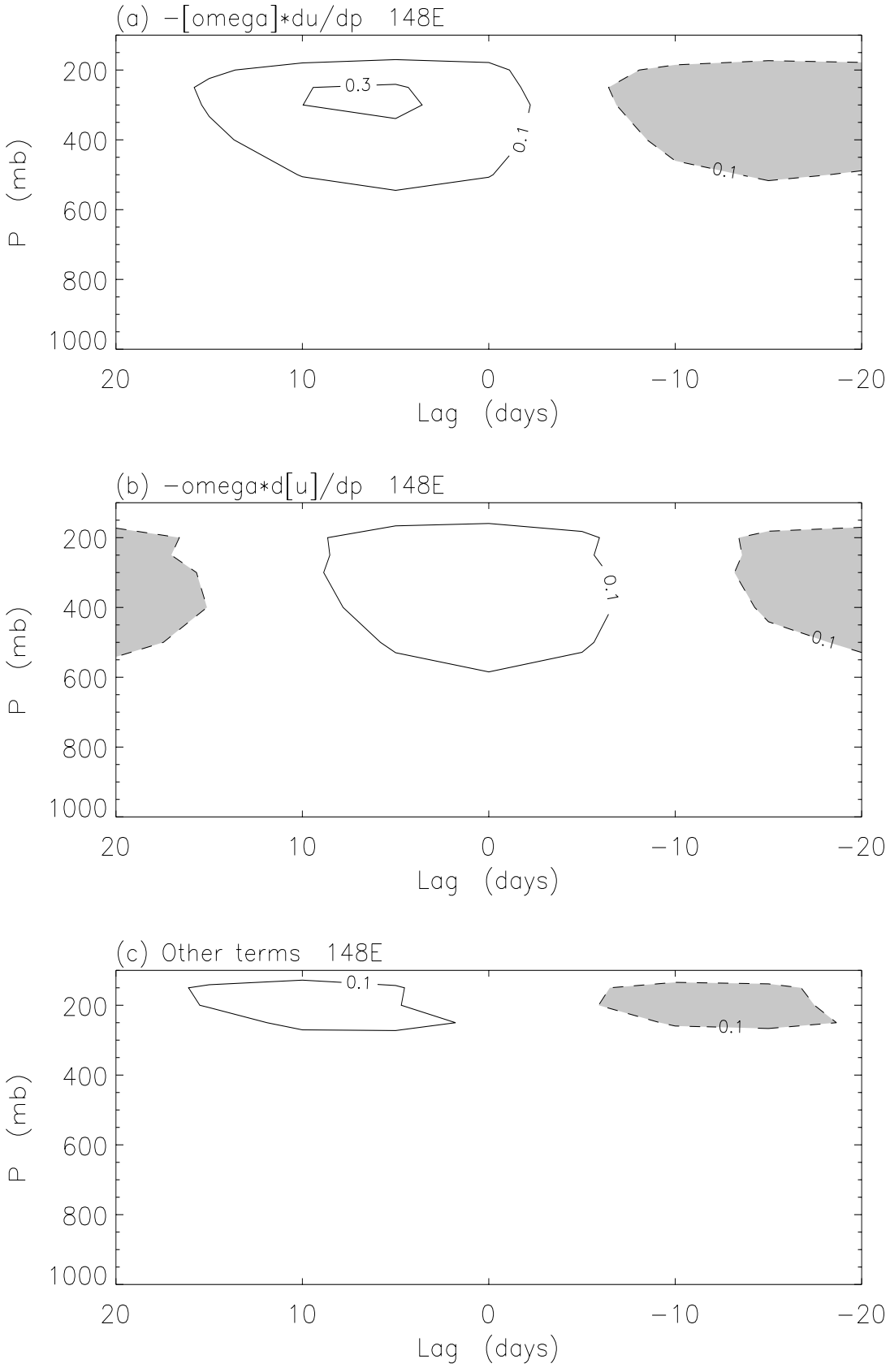
(a) −[omega]*du/dp 148E
0.3
0.1
0.1
P (mb)
200
400
600
800
1000
20
10
0
−10
−20
Lag (days)
(b) −omega*d[u]/dp 148E
0.1
0.1
P (mb)
200
400
600
800
1000
20
10
0
−10
−20
Lag (days)
(c) Other terms 148E
0.1
0.1
P (mb)
200
400
600
800
1000
20
10
0
−10
−20
Lag (days)

Figure 7:

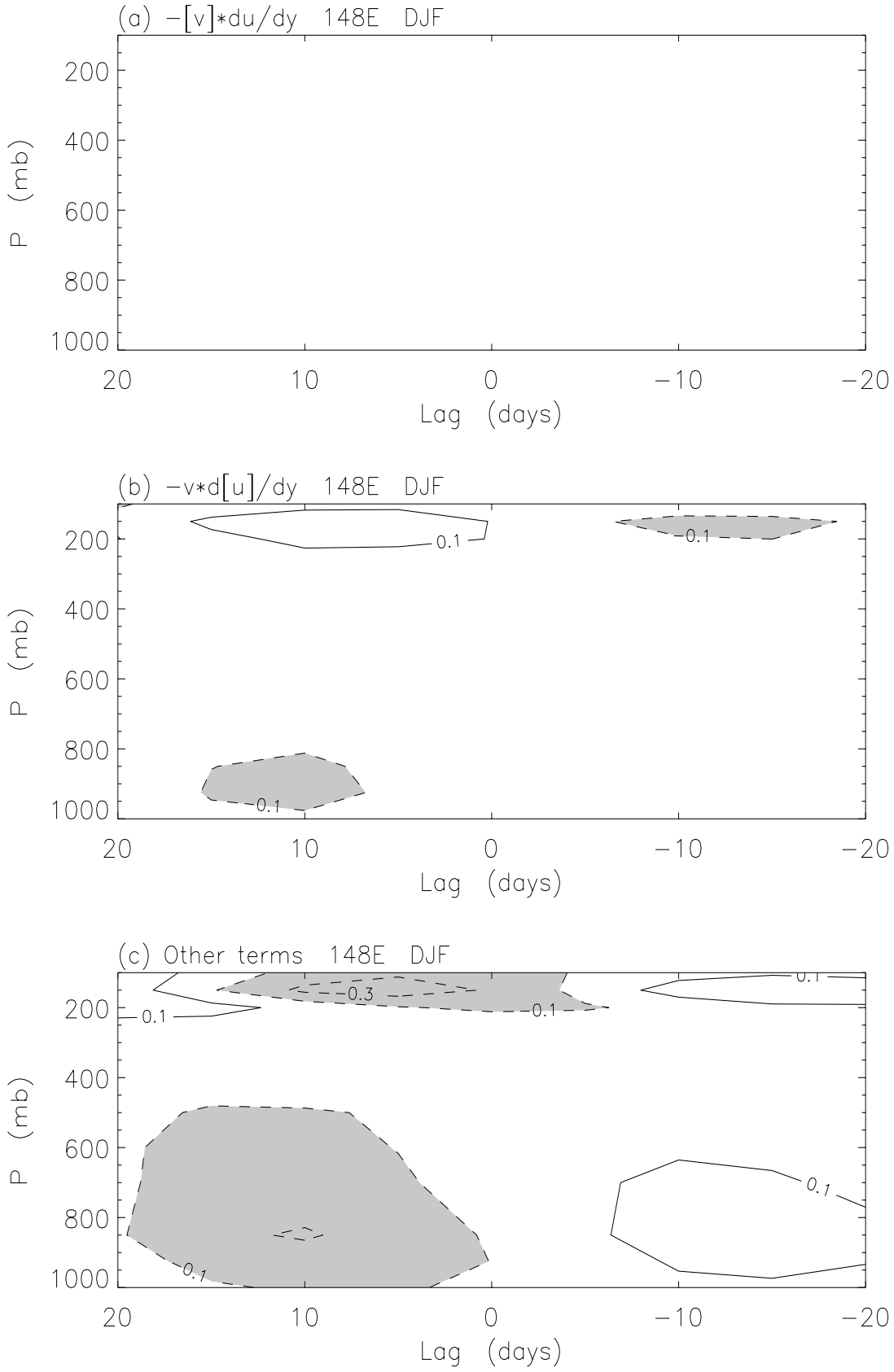
(a) −[v]*du/dy 148E DJF
(b) −v*d[u]/dy 148E DJF
(c) Other terms 148E DJF
P (mb)
200
400
600
800
1000
20
10
0
−10
−20
Lag (days)
0.1
0.3

Figure 8:

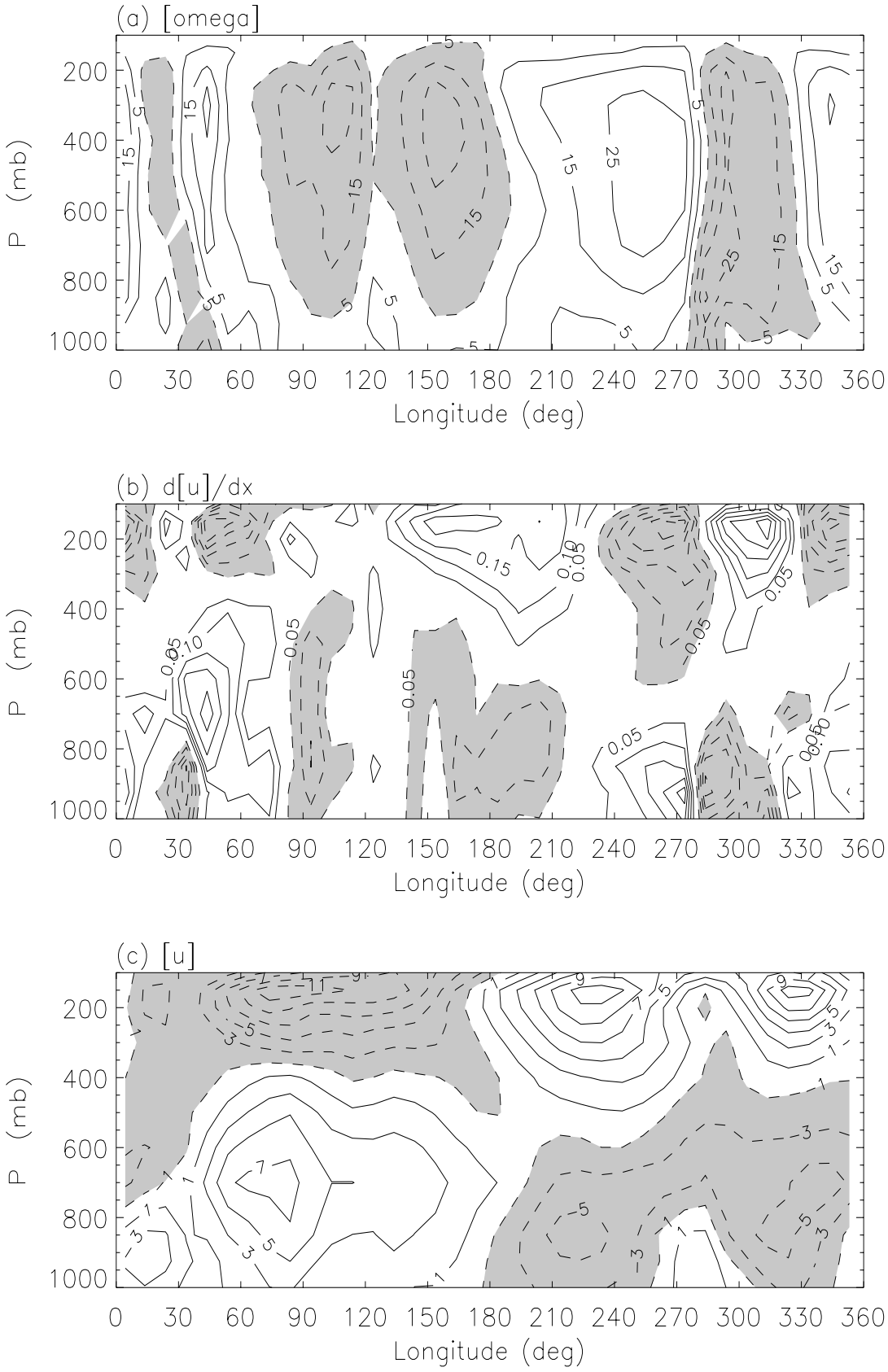
(a) [omega]
P (mb)
200
400
600
800
1000
0 30 60 90 120 150 180 210 240 270 300 330 360
Longitude (deg)
(b) d[u]/dx
P (mb)
200
400
600
800
1000
0 30 60 90 120 150 180 210 240 270 300 330 360
Longitude (deg)
(c) [u]
P (mb)
200
400
600
800
1000
0 30 60 90 120 150 180 210 240 270 300 330 360
Longitude (deg)

Figure 9:

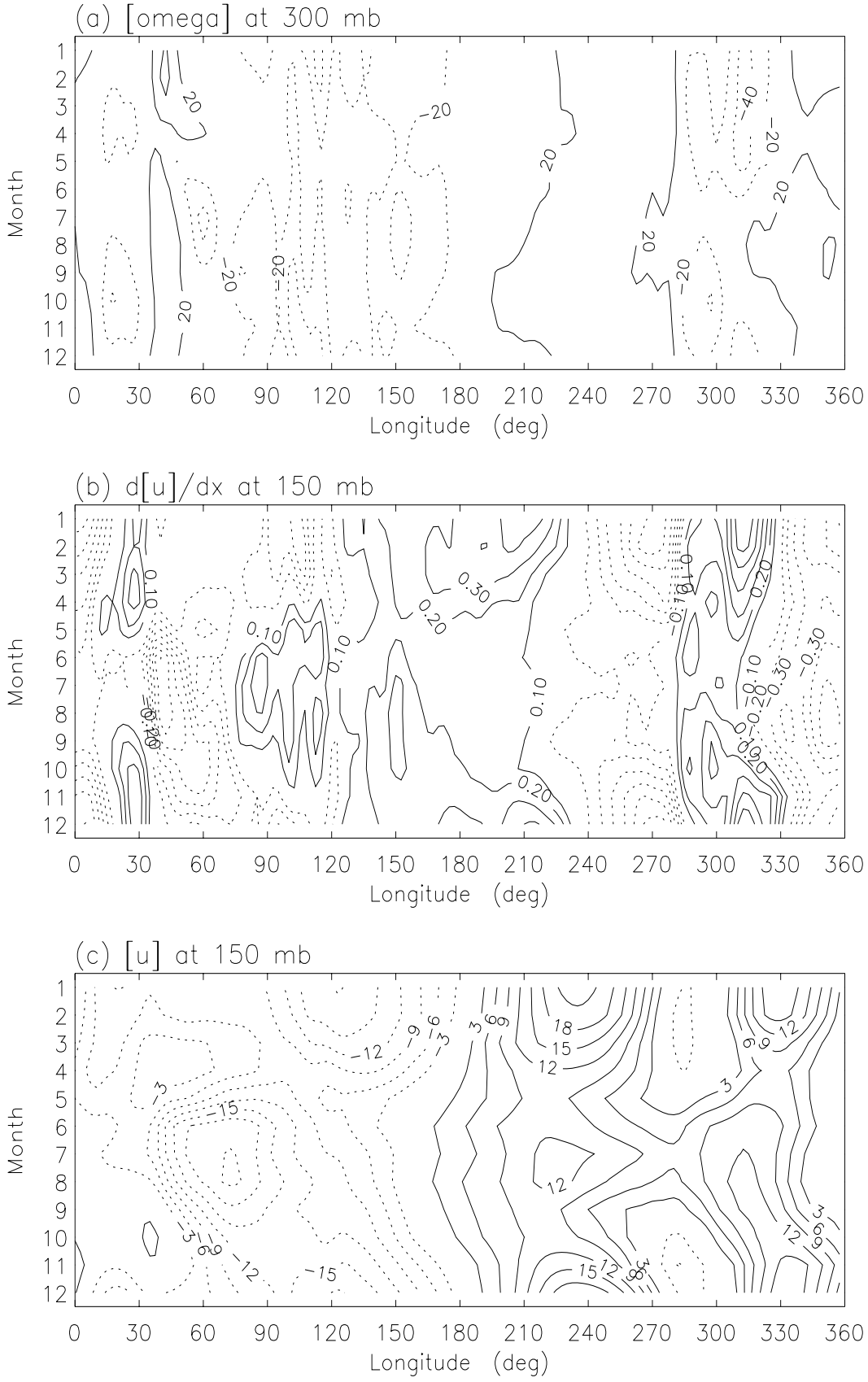
(a) [omega] at 300 mb
(b) d[u]/dx at 150 mb
(c) [u] at 150 mb
Month
Longitude (deg)
0 30 60 90 120 150 180 210 240 270 300 330 360
1 2 3 4 5 6 7 8 9 10 11 12

Figure 10:

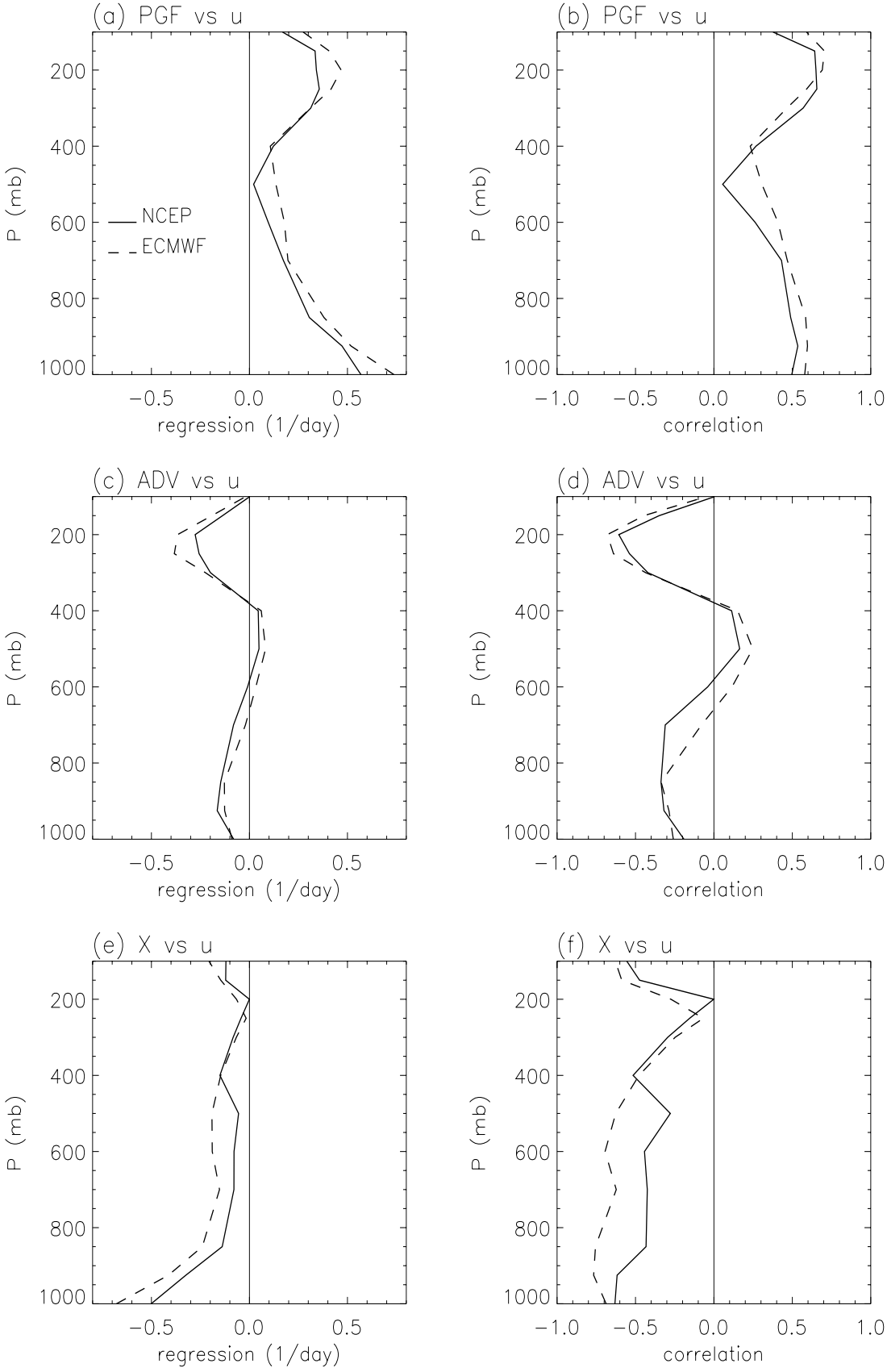
(a) PGF vs u
(b) PGF vs u
(c) ADV vs u
(d) ADV vs u
(e) X vs u
(f) X vs u
P (mb)
200
400
600
800
1000
NCEP
ECMWF
−0.5
0.0
0.5
regression (1/day)
−1.0
1.0
correlation

Figure 11:

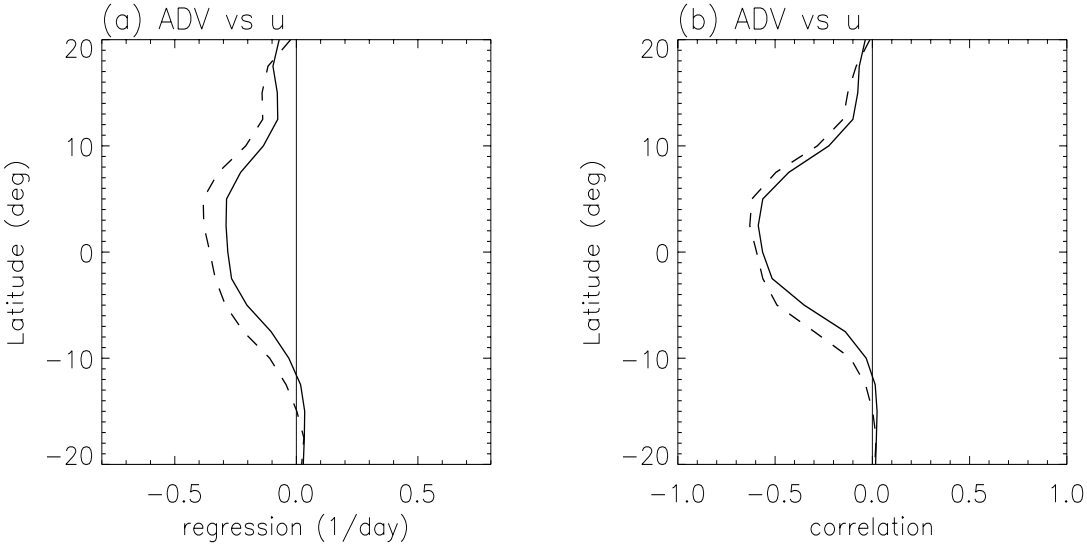
(a) ADV vs u
(b) ADV vs u
Latitude (deg)
20
10
0
−10
−20
−0.5
0.0
0.5
regression (1/day)
−1.0
1.0
correlation

Figure 12:

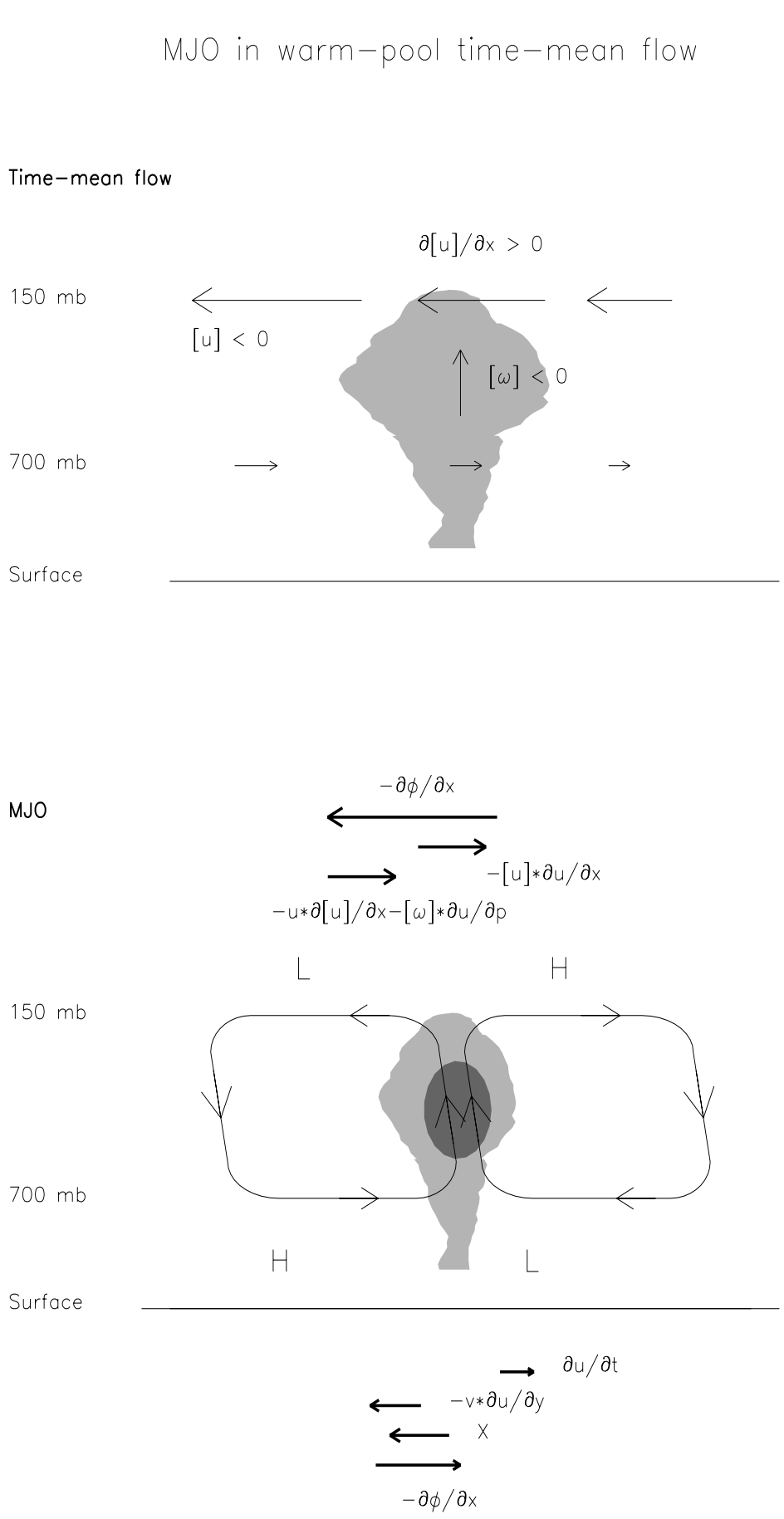
MJO in warm−pool time−mean flow
Time−mean flow
∂[u]/∂x > 0
150 mb
[u] < 0
[ω] < 0
700 mb
Surface
MJO
−∂ϕ/∂x
−[u]∗∂u/∂x
−u∗∂[u]/∂x−[ω]∗∂u/∂p
L
H
150 mb
700 mb
H
L
Surface
∂u/∂t
−v∗∂u/∂y
X
−∂ϕ/∂x

Figure 13: